



Observation of Berry curvature in non-Hermitian system from far-field radiation

Received: 9 August 2024

Accepted: 14 February 2025

Published online: 21 March 2025

Check for updates

Xuefan Yin^{1,2,4}, Ye Chen^{2,4}, Xiaoyu Zhang², Zixuan Zhang², Susumu Noda^① & Chao Peng^{②,3}

Berry curvature that describes local geometrical properties of energy bands can elucidate many fascinating phenomena in solid-state, photonic, and phononic systems, given its connection to global topological invariants such as the Chern number. Despite its significance, the observation of Berry curvature poses a substantial challenge since wavefunctions are deeply embedded within the system. Here, we theoretically propose a correspondence between the geometry of far-field polarization and the underneath band topology in non-Hermitian systems, thus providing a general method to fully capture the Berry curvature without strongly disturbing the eigenstates. We further experimentally observe the Berry curvature in a honeycomb photonic crystal slab from polarimetry measurements and quantitatively obtain the nontrivial valley Chern number. Our work reveals the feasibility of retrieving the bulk band topology from escaping photons and paves the way to exploring intriguing topological landscapes in non-Hermitian systems.

Topology, namely the mathematics of conserved properties under continuous deformations, is creating a range of new opportunities throughout matters, photonics, phononics, and other wave systems^{1–6}. To characterize the topology in physics, the Berry curvature^{7,8} is an essential concept that describes the local, gauge-invariant, geometric manifestation of the wavefunctions in the parameter space, which is closely related to the global topological invariants such as a variety of Chern numbers^{9–13}. However, since Berry curvature belongs to the intrinsic topological property of wavefunctions, it is usually deeply bound inside the system and difficult to observe. Although using tomography can reconstruct the wavefunctions in some particular scenarios^{14,15}, much effort has been devoted to retrieving the Berry curvature from its external consequence in physics. Examples include Hall drift in driving optical lattice^{16–18} or synthetic gauge field^{19,20}, Aharonov–Bohm interference of magnetic-controlled ultracold atom^{21–24}, and pseudospin^{25–30} or dichroism^{31,32} in exciton-polariton-correlated material. Even though the specific physics varies, the mentioned observations of Berry curvature generally rely on the strong light-matter interaction to imprint the topological features of bulk wavefunction to external observables, and thus they should be

categorized into the class of “strong measurement”³³, namely the observation strongly interfering with the system. In comparison, the method of measuring the Berry curvature without much disturbing the eigenstates³⁴ remains absent.

It is well-recognized that open photonic systems necessarily lose photons to their surroundings. As a major route of energy exchange, the far-field radiation naturally carries information about wavefunctions and thus allows direct access to the intrinsic bulk topology, which would be conventionally thought impossible. Here, the escaping photons simply act as the “messengers” that weakly interact with the system, and could bridge the bulk band and radiation. For example, some advances in probing Chern numbers from the far field are reported, in which either phases and intensity³⁵, or frequency and quality factor³⁶ are chosen as observables. However, due to the difficulty in experiments and the lack of degree-of-freedom (DOF), they are probably not ideal observables to enable the direct observation of Berry curvature in general non-Hermitian multi-level photonic systems^{6,37–40}. Hereby we propose that, the far-field polarization is a more applicable candidate because it provides sufficient DOFs, and more importantly, the orientation and ellipticity of polarization can be

¹Department of Electronic Science and Engineering, Kyoto University, Kyoto-Daigaku-Katsura, Nishikyo-ku, Kyoto 615-8510, Japan. ²State Key Laboratory of Photonics and Communications, School of Electronics, & Frontiers Science Center for Nano-optoelectronics, Peking University, Beijing 100871, China. ³Peng Cheng Laboratory, Shenzhen 518055, China. ⁴These authors contributed equally: Xuefan Yin, Ye Chen. e-mail: pengchao@pku.edu.cn

readily and robustly measured in a time-averaging manner. In fact, the nontrivial geometric features of far-field polarization^{41–47} has attracted much attention in recent years because they give rise to interesting physical consequences such as polarization half-charge around paired exceptional point^{48,49}, vortex beam⁵⁰, chiral devices with circular dichroism^{51,52}, bound states in the continuum (BICs)^{53–61} and unidirectional guided resonances (UGRs)^{62–64}. However, the intrinsic connection between the polarization and the bulk wavefunction is still unrevealed, and how to retrieve the Berry curvature from the far-field polarization features still remains an elusive question.

Here we theoretically establish a correspondence between the band topology and radiation geometry to experimentally observe the Berry curvature by characterizing the polarization of escaping photons from a non-Hermitian photonic crystal (PhC) slab system. We prove that, Berry curvatures of bulk bands can be captured by using observable bi-orthogonal polarization vectors in a non-Hermitian system¹⁰. As long as the radiation fields are smooth and well-defined, a full tomography of the Berry curvature can be realized by simply measuring the polarization of a number of radiation channels. Specifically, for a two-level system, only one radiation channel is sufficient. Accordingly, we experimentally observe the nontrivial Berry curvatures originating from the diabolic point (DP) in a honeycomb-lattice PhC slab by using a standard polarimetry measurement⁶⁵. The Berry phases^{2,7,66} of $\gamma - \pm\pi$ are obtained in an individual valley by employing integrals of the observed Berry curvature, showing nontrivial valley-Chern numbers^{11,13} of $C_v^k \sim \pm 1/2$ as expected, and thus quantitatively validate our method.

Results

The bulk-radiation correspondence of the Berry curvature

We start from an infinite two-dimensional (2D) PhC slab operating in the radiation continuum as schematically illustrated in Fig. 1A, which has translational symmetry in both x and y directions. According to the Bloch theorem, the system is ruled by a bulk momentum-space Hamiltonian $\hat{H}(\mathbf{k}_{||})$, supporting multiple bulk Bloch modes whose cell-periodic Bloch function is denoted as $|u_n(\mathbf{k}_{||})\rangle$. The subscript n labels the energy

bands, and $\mathbf{k}_{||}$ is the in-plane Bloch wavevector. Due to the truncation in the z -direction, photons can partially escape from the PhC slab, radiating towards some specific out-of-plane directions owing to the diffraction of periodically modulated permittivity. The far-field radiation in each radiation channel C_q can be formulated by a vector of $|\Psi_{n,q}\rangle = [c_{x,n,q}, c_{y,n,q}]^T$, where $c_{x,y,n,q}$ are complex-valued electric field components of radiative wave in the x and y directions, respectively, and subscript q labels the radiation channel. The field components in s and p directions are discussed in Supplementary Materials section 1.

Generally, as illustrated in Fig. 1A, the radiation vector is characterized by a three-dimensional (3D) wavevector \mathbf{k}_q , which can be decomposed into the in-plane component β_q and the vertical component $k_{z,q} = \sqrt{\omega_n^2/c^2 - |\beta_q|^2}$. Since the radiative waves are diffracted from the Bloch mode, β_q , as well as \mathbf{k}_q , is directly determined from the Bloch wavevector $\mathbf{k}_{||}$. To investigate the connection between bulk Bloch modes and its radiation, we focus on the dependence of radiative waves on the Bloch wavevector $\mathbf{k}_{||}$ rather than the 3D wavevector \mathbf{k}_q . Consequently, at each $\mathbf{k}_{||}$, the radiation process in a given channel C_q can be understood as a linear mapping of $\mathcal{P}_q : |u_n(\mathbf{k}_{||})\rangle \mapsto |\Psi_{n,q}(\mathbf{k}_{||})\rangle = \hat{P}_q(\mathbf{k}_{||})|u_n(\mathbf{k}_{||})\rangle$, governed by a projection matrix denoted as \hat{P}_q . The detailed expressions of β_q with respect to $\mathbf{k}_{||}$ for each channel can be found in Supplementary Materials section 1. In the following discussions, we focus on a single channel, thus omitting the subscript q for simplicity.

The PhC slab we considered here is intrinsically non-Hermitian, due to the existence of radiation losses. Thus, the Berry curvature of the bulk Bloch bands in the 2D Brillouin zone (BZ) can be calculated from the wavefunctions as $B_n(\mathbf{k}_{||}) = i\nabla_{\mathbf{k}_{||}} \times \langle v_n(\mathbf{k}_{||}) | \nabla_{\mathbf{k}_{||}} u_n(\mathbf{k}_{||}) \rangle$, denoted as bulk Berry curvature (bottom panel, Fig. 1B). Here $\langle v_n(\mathbf{k}_{||}) |$ represents the left vector accompanied by the right vector $|u_n(\mathbf{k}_{||})\rangle$, ruled by the bi-orthogonal normalization relation of $\langle v_m(\mathbf{k}_{||}) | u_n(\mathbf{k}_{||}) \rangle = \delta_{mn}$. Accordingly, the right vector $|u_n(\mathbf{k}_{||})\rangle$ can be projected to the radiation vector $|\Psi_n(\mathbf{k}_{||})\rangle$ through the projection matrix \hat{P} . If \hat{P} is an invertible

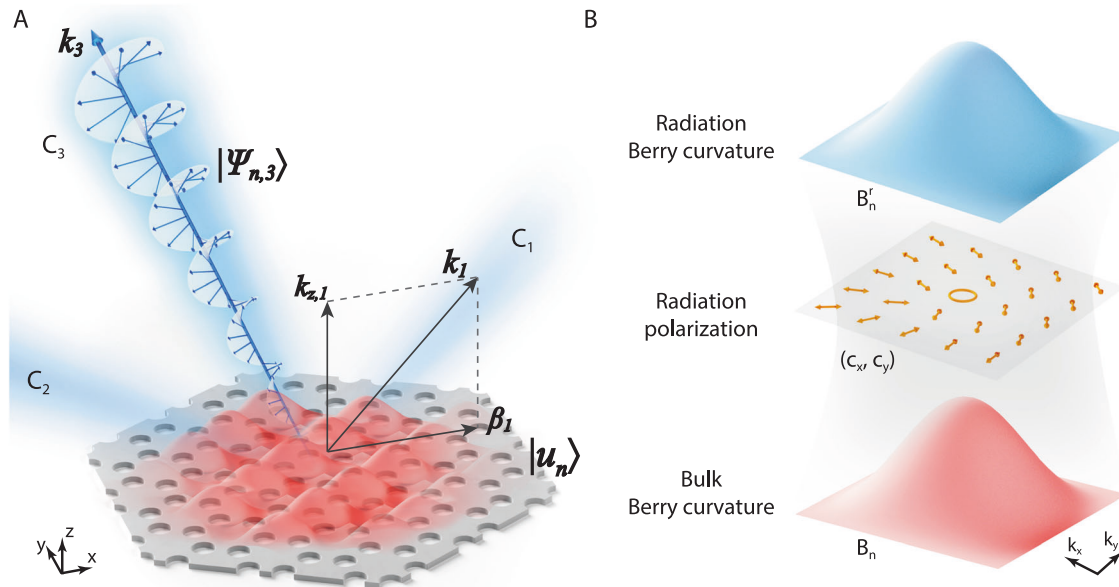


Fig. 1 | Correspondence between bulk band topology and far-field radiation. **A** The schematic of radiation process from the PhC slab to the far field in real space. The wavefunction of the Bloch mode $|u_n\rangle$ in the PhC slab is diffracted by the periodic lattice into several diffraction directions, acting as the radiation channels C_{1-3} . Each channel (i.e., C_3) depends on a 3D wavevector (i.e., \mathbf{k}_3), and can be described by the polarization vector (i.e., $|\Psi_{n,3}\rangle$) marked as the spiral arrows. The 3D wavevector for each channel (i.e., \mathbf{k}_1 for channel C_1) can be decomposed to the

vertical component (i.e., $k_{z,1}$) and in-plane component (i.e., β_1), both determined by the Bloch wavevector $\mathbf{k}_{||}$. **B** The “bulk-radiation correspondence” of Berry curvature in momentum space. The radiation polarization field (middle panel) can bridge the bulk Berry curvature B_n defined in wavefunction $|u_n\rangle$ (bottom panel) with the radiation Berry curvature B_n' defined in far-field radiation vector $|\Psi_n\rangle$ (top panel). $c_{x,y}$ are complex amplitudes of the radiative waves in the x - y plane.

matrix, the left vector $\langle v_n(\mathbf{k}_\parallel) \rangle$ also corresponds to a radiation vector in the term of $\langle \Phi_n(\mathbf{k}_\parallel) \rangle = \langle v_n(\mathbf{k}_\parallel) | \hat{P}^{-1}(\mathbf{k}_\parallel) \rangle$. It is ready to derive that $|\Psi_n\rangle$ and $\langle \Phi_n|$ form another bi-orthogonal basis for the Hamiltonian of $\hat{H}' = \hat{P} \hat{H} \hat{P}^{-1}$, leading to another Berry curvature $B'_n(\mathbf{k}_\parallel) = i \nabla_{\mathbf{k}_\parallel} \times \langle \Phi_n(\mathbf{k}_\parallel) | \nabla_{\mathbf{k}_\parallel} \Psi_n(\mathbf{k}_\parallel) \rangle$ denoted as the “radiation Berry curvature” (top panel, Fig. 1B). We find that B'_n and B_n are related as $B'_n(\mathbf{k}_\parallel) = B_n(\mathbf{k}_\parallel) + i \nabla_{\mathbf{k}_\parallel} \times \langle v_n(\mathbf{k}_\parallel) | \hat{P}^{-1} \nabla_{\mathbf{k}_\parallel} \hat{P} | u_n(\mathbf{k}_\parallel) \rangle$. We further prove that (see Supplementary Materials section 1 for details), in the case that the matrix \hat{P} is smooth and doesn't give rise to extra amplitude vortexes such as BICs that carry zero radiation ($\langle \Psi_n(\mathbf{k}_\parallel) | \Psi_n(\mathbf{k}_\parallel) \rangle = 0$), the second term of B'_n vanishes, and the system follows a simple correspondence between the band topology and radiation topology, given by:

$$B'_n \approx B_n \quad (1)$$

The above equation reveals that the escaping photons project the bulk Berry curvature onto the far-field radiation through the matrix \hat{P} (mid panel, Fig. 1B). Although the wavefunctions $|u_n\rangle$ and $\langle v_n|$ are difficult to access because they belong to the near-field features of bulk Bloch modes, the radiation vectors $|\Psi_n\rangle$ and $\langle \Phi_n|$ are directly observable. Therefore, Eq. (1) offers a possibility to extract the bulk band topology directly from the far-field radiation. The detailed derivation of such a bulk-radiation correspondence can be found in Supplementary Materials section 1. An example that poor-defined \hat{P} collapses the bulk-radiation correspondence is discussed in Supplementary Materials section 2. The physical origin and measurement methods of the left radiation vector $\langle \Phi_n|$ is discussed in the Supplementary Materials section 3.

In theory, the radiation in a particular radiation channel gives a perspective projection of the wavefunctions, and thus it is noteworthy to discuss whether the projection is complete. For a general vector system where N eigen modes exist, the number of internal DOFs of the system is N and both $|u_n\rangle$ and $\langle v_n|$ are N -dimensional vectors. Here we consider the case of $N \geq 2$ since $N = 1$ refers to a scalar single-valuable system and thus only one scalar observable can fully characterize the

system. As we stated above, for each bulk Bloch mode, one radiation channel can only characterize two DOFs ($[c_{x,n}, c_{y,n}]^T$), so \hat{P} should be a $2 \times N$ matrix. For the case with $N > 2$, \hat{P} can't be directly inverted, indicating that a single radiation channel can't provide enough information to depict the bulk wavefunctions, and it's necessary to measure multiple radiation channels simultaneously—observe the same object from different views. As a specific case, if the system is a simple two-level one with $N = 2$, the measurement of only one radiation channel is sufficient to make the projection of wavefunctions complete. Namely, we can reverse the projection process to directly determine the bulk wavefunctions from far-field radiations if \hat{P} is a non-singular invertible 2×2 matrix. In this work, we focus on the simplest $N = 2$ case to present and validate our theory.

Non trivial Berry curvature in honeycomb lattice

To elaborate the correspondence, we consider a 2D PhC slab of Si_3N_4 material with circular air hole patterns on a honeycomb lattice (Fig. 2A). The radii of two air holes in rhombus unit-cell are denoted as r_1 and r_2 , and the lattice constant and slab thickness are denoted as a and h , respectively. The reciprocal lattice is shown in Fig. 2B, where the gray shading area denotes the reduced BZ. According to the Bloch theorem, the wavefunction $|u_n\rangle$ can be expanded as a superposition of a series of quasi-plane waves with discrete momentum, represented by the dots in the reciprocal lattice, and we refer to them as “diffraction orders”⁶⁷. Around the second \mathcal{K} point that resides in the continuum, several diffraction orders fall into the light cone and thus open radiation channels. We take \mathcal{K}_1 point as a specific example, around which exist three radiation channels C_{1-3} (red arrows, Fig. 2B) whose in-plane wavevectors are $\beta_1 = (k_x + \sqrt{3}/3)\beta_0 \mathbf{x}$ and $\beta_{2,3} = (k_x - \sqrt{3}/6)\beta_0 \mathbf{x} + (k_y \mp 1/2)\beta_0 \mathbf{y}$, respectively. Here, k_x and k_y are dimensionless numbers describing the Bloch wavevector \mathbf{k}_\parallel deviating from the \mathcal{K}_1 point, and $\beta_0 = 4\pi/\sqrt{3}a$ is the reciprocal lattice constant. Three quasi-transverse-electric (TE) polarized modes marked as $\text{TE}_{A,B,C}$ with dominated components of (E_x, E_y, H_z) can be found around the \mathcal{K}_1 point due to $C_{6/3}$ symmetry, forming a three-level system with well-separated frequency from the

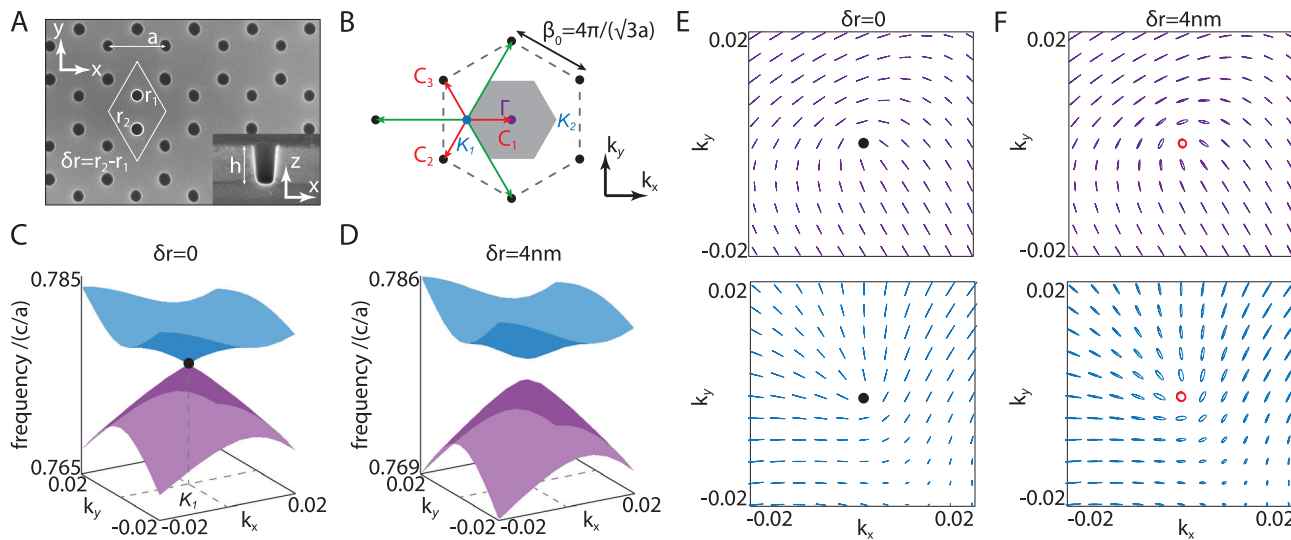


Fig. 2 | Demonstration of Berry curvature observation on a honeycomb-latticed PhC slab. **A** A SEM image of the fabricated PhC sample, showing a honeycomb-lattice structure of SiN slab on SiO_2 substrate with different hole radii. Inset: the side view of the air hole. The structural parameters are given as $a = 440 \text{ nm}$, $r_1 = 50 \text{ nm}$, $r_2 = 54 \text{ nm}$, $h = 180 \text{ nm}$, respectively. δ_r is defined as $r_2 - r_1$. **B** The reciprocal lattice of the PhC sample. Gray shading area: the reduced BZ; purple dot: the Γ point; blue dot: the \mathcal{K}_1 point; red vectors: three diffraction orders acting as radiation channels C_{1-3} ; green vectors: non-radiative diffraction orders. **C, D** The band structures of PhCs around \mathcal{K}_1 point with ($\delta_r = 0$) and without ($\delta_r = 4 \text{ nm}$) the inversion symmetry. Owing to the C_6 symmetry with $\delta_r = 0$, TE_A

mode (purple sheet) and TE_B mode (blue sheet) are degenerate at \mathcal{K}_1 point, giving rise to a DP. When $\delta_r \neq 0$, the DP splits to open a nontrivial bandgap. **E, F** The polarization fields in momentum space of TE_A (purple, the top panels) and TE_B (blue, the bottom panels) modes around \mathcal{K}_1 point with ($\delta_r = 0$) and without ($\delta_r = 4 \text{ nm}$) the inversion symmetry, respectively. For $\delta_r = 0$ with the C_6 symmetry, half charges emerge at \mathcal{K}_1 point due to the DP for both $\text{TE}_{A,B}$ modes. When $\delta_r \neq 0$, two CPs with opposite handedness emerge around the \mathcal{K}_1 point instead. Black dot: DP; red marks: the quasi-CPs. All data are calculated by numerical simulations (COMSOL Multiphysics).

other Bloch modes. For the case that $\delta_r = r_2 - r_1 = 0$ preserving the C_6 symmetry (left panel, Fig. 2C), a twofold degeneracy of TE_A and TE_B right at the K_1 point emerges. As a contrary, $r_1 \neq r_2$ lifts the degeneracy (right panel, Fig. 2D). In the case that the in-plane symmetry breaking is sufficiently weak that allows the coupling from the TE_C mode being neglectable, $TE_{A,B}$ modes form a two-level subsystem near the K_1 point, described by an effective Hamiltonian of:

$$\hat{H}_t = \omega + \delta\sigma_z + \eta k_x\sigma_x + \eta k_y\sigma_y \quad (2)$$

in which ω is the degenerate frequency at K_1 point; $\delta \propto \delta_r$ characterizes the in-plane asymmetry and η is the group velocity. Due to the radiation loss, $\omega = \omega_r + i\gamma_0$ is a complex one, and γ_0 denotes the radiation decay rate. When C_6 symmetry is preserved ($\delta = 0$), the eigenvectors of Eq. (2) can be derived as $|u_n\rangle = [1, \pm |\eta|e^{i\theta}/\eta]^T$ where $e^{i\theta} = (k_x + ik_y)/\sqrt{k_x^2 + k_y^2}$, creating a diabolic point at the K_1 point which is exactly a non-Hermitian counterpart of the Dirac point in Hermitian case, and we still denote it as the DP for short without any confusion.

Degeneracy at DP creates nontrivial bulk band topology. According to Eq. (2), the close form of the theoretical bulk Berry curvature in such a two-level subsystem follows:

$$B_{n,t} = \pm \frac{4\delta\eta^2}{[4\delta^2 + 4\eta^2(k_x^2 + k_y^2)]^{3/2}} \quad (3)$$

where the subscript “*t*” distinguishes $B_{n,t}$ from the B_n while the latter one takes TE_C into account; the signs “ \pm ” denote the two bands $n = A, B$, respectively. Since TE_C mode can be neglected in our case, we have $B_n \approx B_{n,t}$. For a C_6 symmetric system ($\delta = 0$), the bulk Berry curvature shows as a δ -function peaked at the K_1 point ($k_x = k_y = 0$). While for $\delta \neq 0$, the DP splits and opens a topologically nontrivial bandgap, leading to a nontrivial bulk Berry curvature in the vicinity of K_1 point that gives rise to non-zero valley-Chern number.

As we stated above, if the projection matrix \hat{P} doesn't cause extra amplitude vortexes, $B_{n,t}$ can be determined by directly observing the radiation Berry curvature $B_{n,t}^r$ according to bulk-radiation correspondence in Eq. (1). To achieve this, both right and left radiation vectors should be measured. Specifically, the right radiation vector $|\Psi_n\rangle$ corresponds to the far-field polarization:

$$\vec{S}_n = [s_1, s_2, s_3]^T / s_0 = \langle \Psi_n | \hat{\sigma} | \Psi_n \rangle / \langle \Psi_n | \Psi_n \rangle, \text{ where } \hat{\sigma} = [\hat{\sigma}_z, \hat{\sigma}_x, \hat{\sigma}_y]^T$$

are the Pauli's matrices, and \vec{S}_n refers to the Stokes' vector which can be directly measured by using standard polarimetry method⁶⁵. Here we present the simulated polarization vector fields in Fig. 2E, F, showing the footprints of DP in the far-field radiation with the C_6 symmetry. Polarization vortexes can be found in momentum space, each carrying a half-integer topological charge right at the K_1 point (Fig. 2E). Once the symmetry-breaking lifts the degeneracy, the polarization vortexes degrade to a meron-like and anti-meron-like configurations⁶⁸ with circular-polarization (CPs) in opposite helicities around the K_1 point for $TE_{A,B}$ modes, respectively (Fig. 2F). These far-field geometric features can be employed as observable signatures to validate the theory. As for the left radiation vector $(\Phi_m|$, it can be readily determined according to the bi-orthogonal normalization relation of $\langle \Phi_m | \Psi_n \rangle = \delta_{mn}$.

Experimental observation of Berry curvature

To experimentally observe the Berry curvature, we first fabricate the PhC sample by using e-beam lithography (EBL) and inductively coupled plasma etching (ICP) processes on a Si_3N_4 slab of thickness $h = 180$ nm on silica substrate (see Methods section for details). The air holes are arranged as a honeycomb lattice of $a = 440$ nm with two slightly different hole radii of $r_1 = 50$ and $r_2 = 54$ nm, respectively, as the scanning electron microscope (SEM) images shown in Fig. 2A. The angle-resolved measurement system is schematically illustrated in Fig. 3A, in which a supercontinuum white light source is first sent through an acoustic-optic tunable filter (AOTF) and then linearly

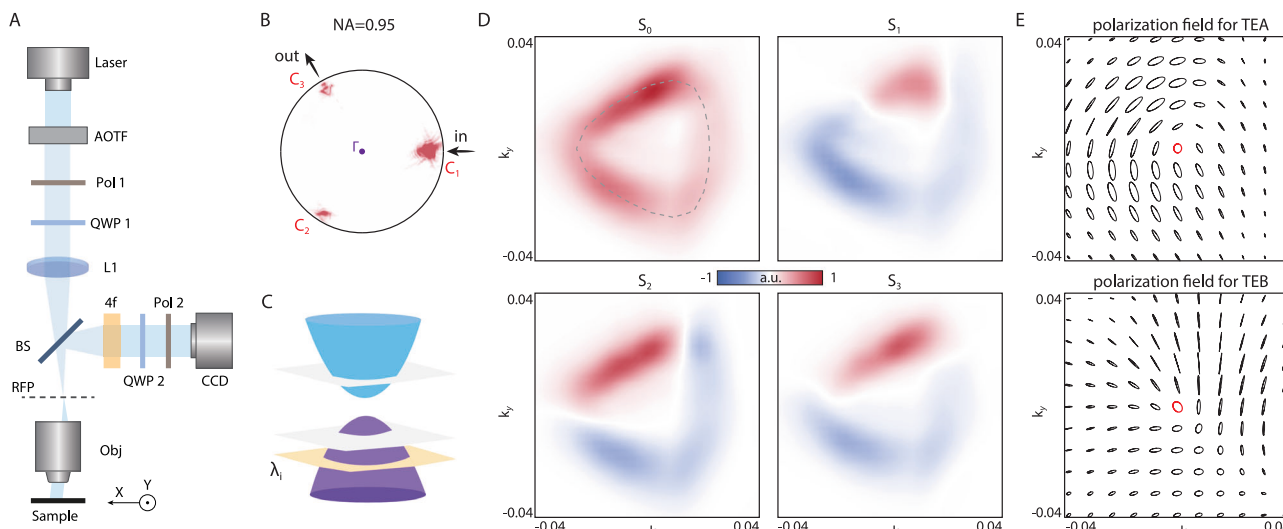


Fig. 3 | Polarimetry measurement of far-field polarization fields. **A** Schematic of the measurements setup. AOTF acoustic-optic tunable filter; POL1 and POL2 polarizers, QWP1 and QWP2 quarter-wave plates, L1 convex lens with 20-cm focal length, BS beam splitter, RFP rear focal plane, Obj objective lens with NA of 0.95 and working distance of 150 μm , 4f lens system with magnification rate of $\times 6$. **B** The observed image of three scattered beams from radiation channels C_{1-3} within the NA range. In the experiment, we excite the optical modes from channel C_1 by moving lens L1 to a proper position and then collect the radiative waves in channel C_3 after it is magnified by the 4f system. **C** Schematic of isofrequency

contours of the two-level system near the K_1 point. The yellow plane denotes the wavelength of $\lambda_i = 570.328$ nm. Purple sheet: TE_A mode; blue sheet: TE_B mode.

D The measured isofrequency contour S_0 and Stokes' parameters S_{1-3} at a wavelength of $\lambda_i = 570.328$ nm. The Stokes' parameters are determined through different configurations of POL2 and QWP2. Dashed line: the simulated isofrequency contour at λ_i . **E** The measured polarization distributions in momentum space around the K_1 point, by overlapping several isofrequency contours and evaluating the overall Stokes' parameters. Red marks: the quasi-CPs.

polarized by POL1 to generate incoherent light in a wavelength range from 550 to 580 nm. After passing through a quarter-wave plate (QWP1), the light is focused by a lens (L1) onto the rear focal plane (RFP) of an infinity-corrected objective lens (NA = 0.95), and then illuminates the sample to excite the optical modes. The radiations from the PhC sample are collected by the same objective lens and imaged by a charge-coupled device (CCD) camera which is co-focused with the RFP of the objective lens. By inserting another polarizer (POL2) and another quarter-wave plate (QWP2) before the CCD, we can fully characterize the Stokes' vector of radiation through a polarimetry method (see Methods section for details).

As shown in Fig. 3B, three scattered beams inside the aperture of the objective lens can be found, corresponding to the radiation channels C_{1-3} plotted in Fig. 2B. As we discussed above, only one radiation channel is sufficient to capture the bulk band topology of the two-level subsystem consisting of $TE_{A,B}$. Therefore, we excite the modes from the C_1 channel and observe them from the C_3 channel to avoid the direct reflected light for a better signal-noise ratio. The C_2 channel is unused. To achieve the best excitation, we fine-tune the incident angle by moving the L1 lens in the $x-y$ plane. Moreover, POL1 and QWP1 are employed to adjust the polarization of incident light: left-handed circular polarization (LCP) for TE_A mode and right-handed circular polarization (RCP) for TE_B mode, respectively. When the AOTF selects a specific wavelength, the scatterings originating from fabrication disorders would make the isofrequency contour at such a wavelength visible due to the on-resonance pumping mechanism^{48,62,69} (Fig. 3C). Then, a cascaded 4f system is applied to zoom-in the contour at a magnification rate of $\times 6$. Further, by recording the CCD images at particular arrangements of POL2 and QWP2 as polarimetry measurements, we can obtain the Stokes' coefficients for each contour. The result at the wavelength of $\lambda_i = 570.328$ nm is presented in Fig. 3D, in which the dashed line is the isofrequency contour calculated from numerical simulation for visual guidance. By overlapping all the isofrequency contours in the wavelength range of 559.383 – 564.861 nm for the TE_A band and 565.203 – 571.352 nm for the TE_B band, we obtain the polarization vector fields for both $TE_{A,B}$ bands (Fig. 3E). In the vicinity of the K_1 point, an LCP and an RCP can be found on the TE_A and

TE_B bands, respectively (red circles, Fig. 3E), which agree well with our prediction in simulation as shown in Fig. 2F.

The radiation Berry curvature $B_{n,t}^r$ can be directly obtained from the polarization vector fields measured from channel C_3 . Here we consider four samples with radius differences of $\delta_r = 0, 4, 7, 10$ nm, and measure the $B_{A,B,t}^r$ of each sample (top panels, Fig. 4). As a comparison, we numerically calculate the bulk Berry curvature $B_{A,B}$ by employing the semi-analytical coupled-wave theory framework^{56,70,71} (bottom panels, Fig. 4). To better show the evolution of Berry curvatures, we plot the unit-cell geometry of each sample and the corresponding band structures of $TE_{A,B}$ as the insets in the top and bottom panels of Fig. 4. Specifically, we start from a realistic sample with $\delta_r = 0$ (Fig. 4A), where the fabrication imperfections would inevitably break the DP degeneracy at K_1 point and give rise to a very small bandgap. We estimate that the bandgap is equivalent to the case of $\delta_r = 2$ nm. In this case, we found that the $B_{A,B,t}^r$ show as bright spots centered at K_1 point—quite like δ -functions (top panels, Fig. 4A), agreeing well with the numerical bulk Berry curvatures $B_{A,B}$ (bottom panels, Fig. 4A). Note that the signs of $B_{A,t}^r$ and $B_{B,t}^r$ are exactly opposite, agreeing well with the theoretical prediction in Eq. (3). Further, we gradually open the bandgap by increasing δ_r from 4 to 10 nm (Fig. 4B). During this process, the Berry curvatures $B_{B,t}^r$ and B_B both gradually diffuse to a larger region in momentum space while their peak absolute values decrease. At $\delta_r = 10$ nm, the bandgap becomes quite large, and thus both $B_{n,t}^r$ and B_n become fully dispersed and no longer congregate around K_1 point. $B_{A,t}^r$ and B_A also match well with each other and have similar behaviors (see Methods section). The great agreement between the experimentally observed radiation Berry curvatures $B_{A,B,t}^r$ and the numerically calculated bulk Berry curvature $B_{A,B}$ confirms the bulk-radiation correspondence we propose in Eq. (2). It's noteworthy that Berry curvatures are generally complex values in a non-Hermitian system. For our PhC slab in which only radiation contributes to the non-Hermiticity, the imaginary parts of Berry curvature are quite small compared to their real parts (see Supplementary Materials section 1 for details).

To further quantitatively validate the bulk-radiation correspondence, we calculate the geometric phases (Berry phases) $\gamma_{n,t}^r$ and γ_n by applying 2D integrals over the radiation (measured) and bulk

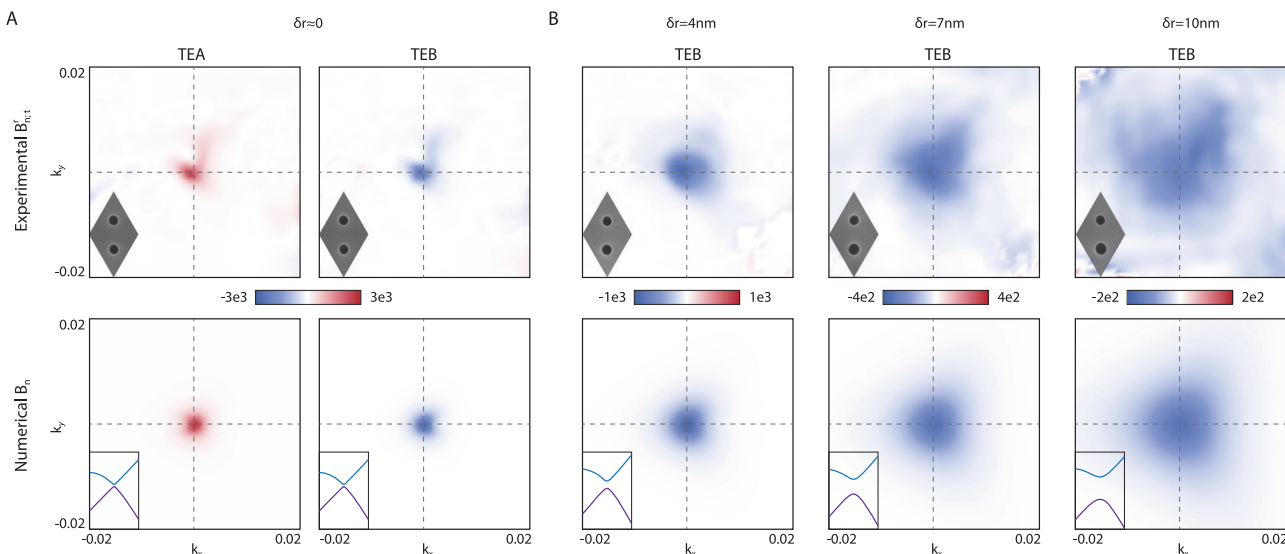


Fig. 4 | Experimental observation of Berry curvatures. **A** The measured radiation Berry curvatures $B_{n,t}^r$ for the PhC sample with $\delta_r \approx 0$ (top panels) and the numerically calculated bulk Berry curvatures B_n with $\delta_r = 2$ nm (bottom panels) for a comparison. For a realistic sample with $\delta_r = 0$, the fabrication errors would slightly lift the DP at K_1 point to create a small bandgap. We estimate that the bandgap is equivalent to the case of $\delta_r = 2$ nm. In this case, the Berry curvatures congregate around the K_1 point since the bandgap is very small, showing opposite signs for

TE_A and TE_B modes. **B** The measured radiation Berry curvatures $B_{n,t}^r$ (top panels) and the numerically calculated bulk Berry curvatures B_n (bottom panels) for TE_B mode when $\delta_r = 4$ nm (left), 7 nm (middle), and 10 nm (right). Along with the increasing δ_r , the bandgap gradually opens, and the Berry curvature gradually diffuses to a larger region in momentum space. Insets in top panels: SEM images of the unit cell of each PhC sample; insets in bottom panels: band structures of the two-level system accordingly.

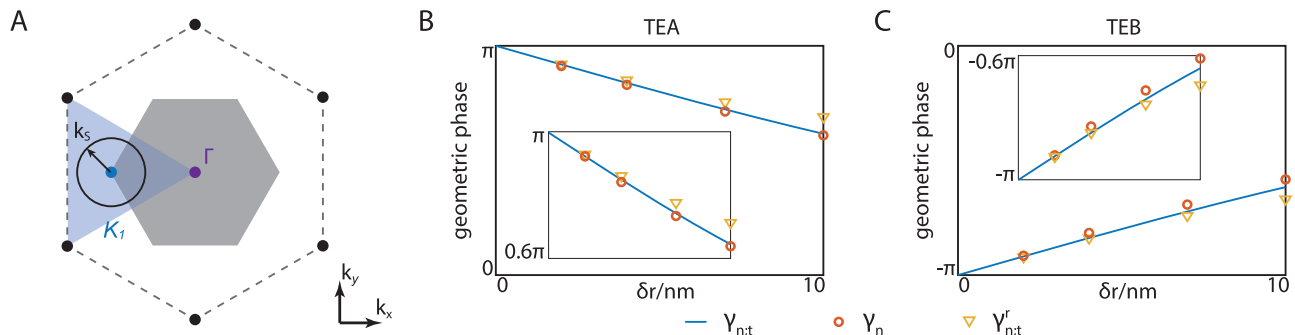


Fig. 5 | Geometric phases obtained from measured Berry curvatures.

A Schematic of an individual valley (blue shading) around the K_1 point (blue dot) in the reciprocal lattice. The integral on Berry curvature over the individual valley gives the geometric (Berry) phases. Considering that the Berry curvatures congregate around the K_1 point when δ_r is relatively small, we perform the integral on a circular region (black circle) to simplify the calculation. Gray shading: the first BZ; purple dot: the Γ point; blue dot: the K_1 point. **B, C** The geometric phases for $TE_{A,B}$ modes. Blue solid line: theoretical bulk Berry phase $\gamma_{n,t}$ of the two-level model according to Eq. (4); red circles: numerical bulk Berry phase γ_n obtained from the

integral of bulk Berry curvatures B_n calculated in Fig. 4; yellow triangles: geometric phase $\gamma_{n,t}^r$ obtained from measured radiation Berry curvature $B_{n,t}^r$ shown in Fig. 4. When $\delta_r = 0$, the theoretical Berry phases are exactly $\pm\pi$ for $TE_{A,B}$ modes owing to the existence of DP, corresponding to quantized valley-Chern numbers of $\pm 1/2$. When δ_r gradually increases, all the geometric phases gradually deviate from the quantized $\pm\pi$. Moreover, when δ_r becomes relatively large, the theoretical $\gamma_{n,t}$ and measured $\gamma_{n,t}^r$ slightly deviate from the numerical γ_n , due to the impact of TE_C mode.

(numerical) Berry curvatures of $B_{n,t}^r$ and B_n in Fig. 4, respectively. As a reference, we also derive the analytic expression of geometric phase $\gamma_{n,t}$ according to Eq. (3), in which the contribution of TE_C band is neglected:

$$\gamma_{n,t} = \pm \left(\pi - \frac{2\delta}{\sqrt{4\delta^2 + 4\eta^2 k_s^2}} \pi \right) \quad (4)$$

According to valleytronics¹¹, the integral of Berry curvature upon the individual valley region determines the valley-Chern number (blue shading, Fig. 5A). Considering that the nontrivial Berry curvatures congregate around the K_1 point, here we choose a circular integral region with radius of $k_s = 0.03$ for simplicity and thus calculate $\gamma_{n,t}^r$ (triangle), γ_n (circle), and $\gamma_{n,t}$ (solid line) shown in Fig. 5B, C. According to Eq.(4), the analytic geometric phases $\gamma_{n,t}$ exactly equals to $\pm\pi$ at $\delta_r = 0$ for $TE_{A,B}$ bands⁷², corresponding to the nontrivial quantized valley-Chern number of $C_v^K = \pm 1/2$ in an individual valley¹¹. When $\delta_r \neq 0$, the open bandgap (nonzero δ) would make the geometric phases deviate from $\pm\pi$, unless the integral region k_s tends to be infinite². Our experimental observation verifies such a behavior. For instance, at $\delta_r = 10$ nm, we obtain $\gamma_{n,t}^r \approx \pm 0.7\pi$ deviated from $\pm\pi$ due to the impact of nonzero bandgap. On the other hand, we find the three geometric phases $\gamma_{n,t}^r$, γ_n and $\gamma_{n,t}$ agree well with each other when δ_r is relatively small, quantitatively proving the validity of bulk-radiation correspondence. For a large δ_r , both analytic geometric phase $\gamma_{n,t}$ solved from the two-level model and the measured $\gamma_{n,t}^r$ from radiation slightly deviate from the bulk Berry phase γ_n , due to the exclusion of the third TE_C band. Because the TE_C mode also contributes to far-field radiation, the deviation upon $\gamma_{n,t}^r$ is more notable than that upon $\gamma_{n,t}$. Actually, we found $\gamma_{n,t}^r < \gamma_{n,t} \lesssim \gamma_n$ for TE_B mode. To improve the measurement accuracy for large δ_r , TE_C mode can't be neglected, and we need to measure the polarization distributions from two independent radiation channels (i.e., C_3 and C_2) to completely capture the information of the three-level system with higher DOFs ($N = 3$). The exemplary example and more discussions are presented in Supplementary Materials section 4 and 5.

Discussion

We emphasize that although the non-Hermiticity in our exemplary system doesn't give rise to nontrivial topological effects, the system is

still intrinsically non-Hermitian due to the radiation loss, and hence, its mathematical structure must follow a bi-orthogonal relation of left and right vectors together. This indicates that the far-field observables must provide sufficient DOFs to solve the Berry curvatures. Compared to the observables such as wavelength and Q -factor, which are only associated with the complex frequencies of Bloch modes, the far-field polarization is a direct projection of the wavefunction itself that naturally presents the information about it (see Supplementary Materials section 4 for details). Therefore, we conclude that the polarizations should be a better candidate to measure the Berry curvature. Our theory and method are valid for general non-Hermitian photonic systems, even with multi-internal DOFs, as long as the measurable radiation exists.

In the experiment stated above, we directly measure the two right vectors $|\Psi_{A,B}\rangle$ at the \mathbf{k}_\parallel point and obtain the left vectors $\langle\Phi_{A,B}|$ by using the bi-orthogonal normalization relation. However, the left vector can also be directly measured. According to the law of reciprocity, the left radiation vector at the \mathbf{k}_\parallel point would correspond to the right radiation vector at the $-\mathbf{k}_\parallel$ point (see Supplementary Materials section 3 for details). Therefore, one can also observe one band at both \mathbf{k}_\parallel and $-\mathbf{k}_\parallel$ points to retrieve the system's topology, instead of measuring two bands simultaneously.

Our findings reveal that the radiation polarization does contain the fingerprint of bulk topology described by the Berry curvature upon a bi-orthogonal basis, but it remains elusive whether all the topological features in the far-field originate from the band topology. Our short-cut answer is negative. Specifically, different from the Berry curvature depending on bi-orthogonal basis, we can also define a "right-right" curvature of $B_{n,r}^r = i\nabla_{\mathbf{k}_\parallel} \times \langle\Psi_n(\mathbf{k}_\parallel)|\nabla_{\mathbf{k}_\parallel}\Psi_n(\mathbf{k}_\parallel)\rangle$ upon the right radiation vector $|\Psi_n\rangle$ only⁴⁰, capturing the geometric features of the polarization field itself. In fact, the integral over "right-right" curvature presents the Pancharatnam-Berry (PB) phase^{73–76} of far-field polarization, showing the swirling structure of Stokes' vector \vec{S}_n in momentum space. We note that, nontrivial polarization features of meron and anti-meron in Fig. 3E don't correspond to the valley-Chern number of bulk topology but are related to the Skyrmiion numbers^{77–79} given by the PB phases (see Supplementary Materials section 6 for details).

In summary, our findings of "bulk-radiation correspondence" of Berry curvature reveal the feasibility of retrieving the band topology from characterizing far-field radiation. We prove in theory and demonstrate in experiments that employing the polarizations of one

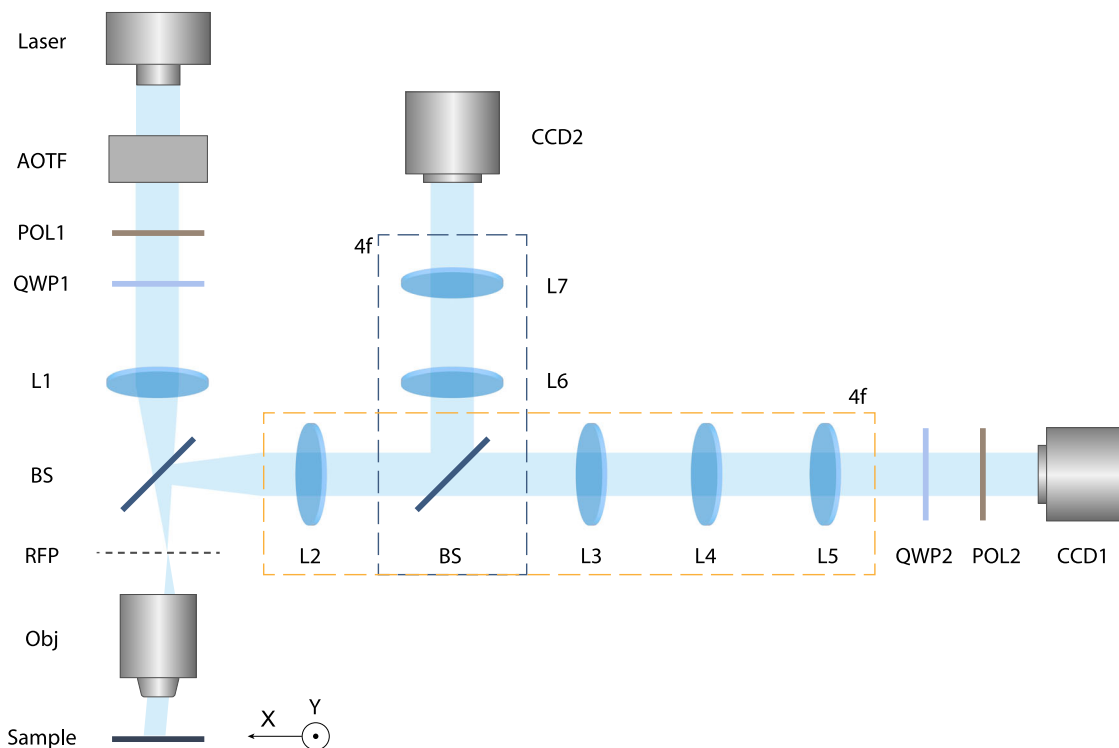


Fig. 6 | The experiment setup. The focal lengths of lenses L1, L2, L3, L4, L5, L6, and L7 are 300, 200, 300, 75, 300, 200, and 125 mm, respectively. AOTF acoustic-optic tunable filter, POL polarizer, QWP quarter-wave plate, BS beam splitter, RFP rear focal plane, Obj objective lens (50X and NA = 0.95), CCD charge-coupled device.

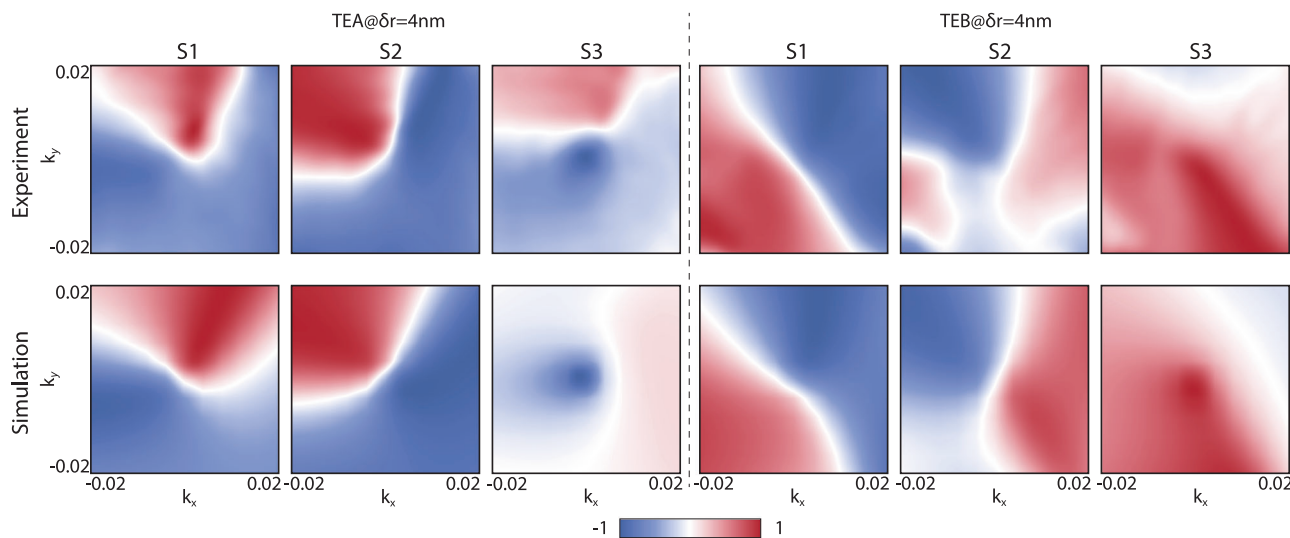


Fig. 7 | Measured and simulated Stokes' parameters for PhC slab of $\delta_r = 4 \text{ nm}$. Left panels: Measured (top panels) and simulated (bottom panels) Stokes' parameters (S_{1-3}) for TE_A mode when $\delta_r = 4$; Right panels: Measured (top panels) and

simulated (bottom panels) Stokes' parameters (S_{1-3}) for TE_B mode when $\delta_r = 4$. For both two modes, the experiment results agree well with the simulated ones.

radiation channel can accomplish a complete map of wavefunctions in a two-level non-Hermitian system, to directly access the Berry curvature and Chern number without strongly disturbing the system. The proposed method can also be extended to multi-level systems by measuring more radiation channels simultaneously, and utilized to extract other topological features such as quantum geometric tensor^{25–28,80,81}. Our work demonstrates a simple and effective way of directly observing the Berry curvature in non-Hermitian systems and thus could shed light on the exploration of the intriguing phases in topological systems.

Methods

Sample fabrication

A LPCVD deposited $\text{Si}_3\text{N}_4\text{-SiO}_2\text{-Si}$ wafer with 1- μm -thick lower cladding of SiO_2 was used. The pattern was defined by electron-beam lithography (EBL). The sample was firstly spin-coated with ZEP520A photoresist, followed by exposure to EBL (Elionix ELS-F125G8) at the current of 1 nA and field size of 500 μm . After the exposure, the sample was etched with inductively coupled plasma (ICP, Oxford) by a mixture of CHF_3 and O_2 . The ICP etching time and chamber pressure are carefully controlled for etching depth and smooth side walls.

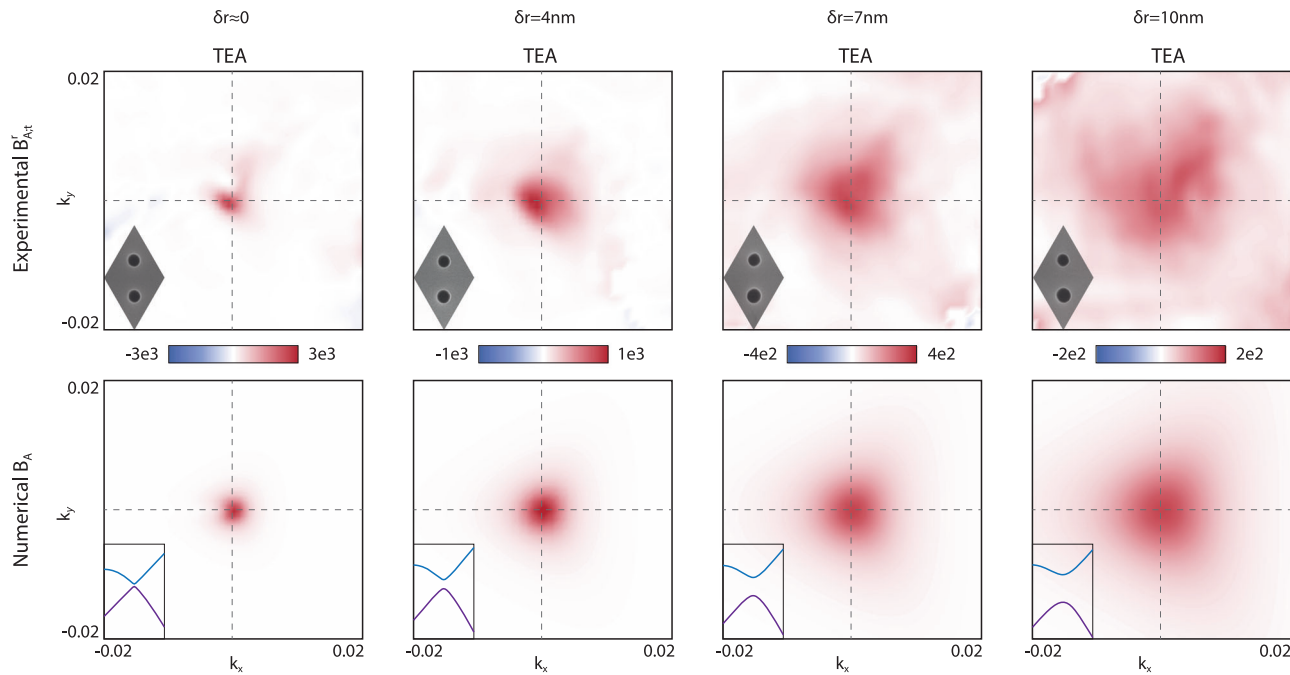


Fig. 8 | Experimental observation of Berry curvatures for TE_A mode. Top panels: Measured radiation Berry curvature $B_{A,r}^r$ when $\delta_r \approx 0$ (the first from left), $\delta_r = 4 \text{ nm}$ (the second from left), 7 nm (the third from left), and 10 nm (right). Bottom panels:

(the second from left), 7 nm (the third from left), and 10 nm (right). The experimental results agree well with the simulated ones. Along with the increasing δ_r , the bandgap between TE_A mode and TE_B mode increases, and the Berry curvatures gradually diffuse to a larger region in momentum space.

Measurements

As shown in Fig. 6, the supercontinuum light source (SuperK Compact; NKT Photonics) is broadband in the range of 450–2400 nm. The incident light is followed by an acoustic-optic tunable filter (AOTF; Gooch & Housego) to scan and pick up the resonance wavelength. After passing through a polarizer (POL1) and a quarter-wave plate (QWP1), the incident light is focused by a lens (L1) onto the rear focal plane (RFP) of the objective lens for exciting the sample. We control the incident light to be left-handed and right-handed circular polarized by arranging POL1 and QWP1 to excite TE_A and TE_B bands, respectively. The radiation field of the sample, collected by the objective lens, is magnified by a two-stage 4f system (L2–L5) and passes through a quarter-wave plate (QWP2) and a polarizer (POL2) before observed by a CCD camera (CCD1). Another 4f system (L6–L7) and camera (CCD2) are used to monitor the near field of the sample surface. We perform polarimetry measurement of the diffraction from the C_3 radiation channel by six configurations of QWP2 and POL2: (1) no QWP2, POL2 oriented along the x -axis; (2) no QWP2, POL2 oriented along the y -axis; (3) no QWP2, POL2 oriented at 45° with respect to the x -axis; (4) QWP2 fast axis fixed along y -axis, POL2 oriented at 45° with respect to the x -axis; (5) no QWP2, POL2 oriented at 135° with respect to the x -axis; (6) QWP2 fast axis fixed along y -axis, POL2 oriented at 135° with respect to the x -axis. The far-field images are recorded by a CCD camera for further processing.

Measurement results of the Stokes' parameters

We present the measurement results of the Stokes' parameters of both TE_A and TE_B bands for the PhC slab of $\delta_r = 4 \text{ nm}$, shown in Fig. 7. The experiment and the simulation results match well with each other.

Berry curvature for TE_A band

We present the evolution of measured radiation Berry curvature for TE_A band when δ_r varies in Fig. 8. Also, the experiment results agree well with the simulation results (bulk Berry curvature).

Data availability

All data needed to evaluate the conclusions in the paper are present in the paper and the supplementary materials.

References

- Hasan, M. Z. & Kane, C. L. Colloquium: topological insulators. *Rev. Mod. Phys.* **82**, 3045 (2010).
- Xiao, D., Chang, M.-C. & Niu, Q. Berry phase effects on electronic properties. *Rev. Mod. Phys.* **82**, 1959 (2010).
- Lu, L., Joannopoulos, J. D. & Soljačić, M. Topological photonics. *Nat. Photon.* **8**, 821–829 (2014).
- Khanikaev, A. B. & Shvets, G. Two-dimensional topological photonics. *Nat. Photon.* **11**, 763–773 (2017).
- Ozawa, T. et al. Topological photonics. *Rev. Mod. Phys.* **91**, 015006 (2019).
- Bergホltz, E. J., Budich, J. C. & Kunst, F. K. Exceptional topology of non-hermitian systems. *Rev. Mod. Phys.* **93**, 015005 (2021).
- Berry, M. V. Quantal phase factors accompanying adiabatic changes. *Proc. R. Soc. A* **392**, 45–57 (1984).
- Haldane, F. D. M. Berry curvature on the fermi surface: anomalous hall effect as a topological fermi-liquid property. *Phys. Rev. Lett.* **93**, 206602 (2004).
- Thouless, D. J., Kohmoto, M., Nightingale, M. P. & den Nijs, M. Quantized hall conductance in a two-dimensional periodic potential. *Phys. Rev. Lett.* **49**, 405 (1982).
- Sheng, D., Weng, Z., Sheng, L. & Haldane, F. Quantum spin-hall effect and topologically invariant chern numbers. *Phys. Rev. Lett.* **97**, 036808 (2006).
- Xiao, D., Yao, W. & Niu, Q. Valley-contrasting physics in graphene: magnetic moment and topological transport. *Phys. Rev. Lett.* **99**, 236809 (2007).
- Zhang, F., Jung, J., Fiete, G. A., Niu, Q. & MacDonald, A. H. Spontaneous quantum hall states in chirally stacked few-layer graphene systems. *Phys. Rev. Lett.* **106**, 156801 (2011).

13. Zhang, F., MacDonald, A. H. & Mele, E. J. Valley chern numbers and boundary modes in gapped bilayer graphene. *Proc. Natl Acad. Sci. USA* **110**, 10546–10551 (2013).
14. Hauke, P., Lewenstein, M. & Eckardt, A. Tomography of band insulators from quench dynamics. *Phys. Rev. Lett.* **113**, 045303 (2014).
15. Fläschner, N. et al. Experimental reconstruction of the berry curvature in a floquet bloch band. *Science* **352**, 1091–1094 (2016).
16. Price, H. M. & Cooper, N. Mapping the berry curvature from semi-classical dynamics in optical lattices. *Phys. Rev. A* **85**, 033620 (2012).
17. Jotzu, G. et al. Experimental realization of the topological haldane model with ultracold fermions. *Nature* **515**, 237–240 (2014).
18. Aidelsburger, M. et al. Measuring the chern number of hofstadter bands with ultracold bosonic atoms. *Nat. Phys.* **11**, 162–166 (2015).
19. Ozawa, T. & Carusotto, I. Anomalous and quantum hall effects in lossy photonic lattices. *Phys. Rev. Lett.* **112**, 133902 (2014).
20. Wimmer, M., Price, H. M., Carusotto, I. & Peschel, U. Experimental measurement of the berry curvature from anomalous transport. *Nat. Phys.* **13**, 545–550 (2017).
21. Abanin, D. A., Kitagawa, T., Bloch, I. & Demler, E. Interferometric approach to measuring band topology in 2d optical lattices. *Phys. Rev. Lett.* **110**, 165304 (2013).
22. Atala, M. et al. Direct measurement of the zak phase in topological bloch bands. *Nat. Phys.* **9**, 795–800 (2013).
23. Duca, L. et al. An Aharonov-Bohm interferometer for determining bloch band topology. *Science* **347**, 288–292 (2015).
24. Li, T. et al. Bloch state tomography using Wilson lines. *Science* **352**, 1094–1097 (2016).
25. Bleu, O., Solnyshkov, D. & Malpuech, G. Measuring the quantum geometric tensor in two-dimensional photonic and exciton-polariton systems. *Phys. Rev. B* **97**, 195422 (2018).
26. Gianfrate, A. et al. Measurement of the quantum geometric tensor and of the anomalous hall drift. *Nature* **578**, 381–385 (2020).
27. Ren, J. et al. Nontrivial band geometry in an optically active system. *Nat. Commun.* **12**, 689 (2021).
28. Liao, Q. et al. Experimental measurement of the divergent quantum metric of an exceptional point. *Phys. Rev. Lett.* **127**, 107402 (2021).
29. Polimeno, L. et al. Tuning of the berry curvature in 2d perovskite polaritons. *Nat. Nanotechnol.* **16**, 1349–1354 (2021).
30. Łempicka-Mirek, K. et al. Electrically tunable berry curvature and strong light-matter coupling in liquid crystal microcavities with 2d perovskite. *Sci. Adv.* **8**, eabq7533 (2022).
31. Wu, S. et al. Electrical tuning of valley magnetic moment through symmetry control in bilayer mos2. *Nat. Phys.* **9**, 149–153 (2013).
32. Cho, S. et al. Experimental observation of hidden berry curvature in inversion-symmetric bulk 2 h- wse 2. *Phys. Rev. Lett.* **121**, 186401 (2018).
33. Vallone, G. & Dequal, D. Strong measurements give a better direct measurement of the quantum wave function. *Phys. Rev. Lett.* **116**, 040502 (2016).
34. Dressel, J., Malik, M., Miatto, F. M., Jordan, A. N. & Boyd, R. W. Colloquium: understanding quantum weak values: basics and applications. *Rev. Mod. Phys.* **86**, 307 (2014).
35. Leykam, D. & Smirnova, D. A. Probing bulk topological invariants using leaky photonic lattices. *Nat. Phys.* **17**, 632–638 (2021).
36. Gorlach, M. A. et al. Far-field probing of leaky topological states in all-dielectric metasurfaces. *Nat. Commun.* **9**, 909 (2018).
37. Feng, L., El-Ganainy, R. & Ge, L. Non-hermitian photonics based on parity-time symmetry. *Nat. Photon.* **11**, 752–762 (2017).
38. Leykam, D., Bliokh, K. Y., Huang, C., Chong, Y. D. & Nori, F. Edge modes, degeneracies, and topological numbers in non-hermitian systems. *Phys. Rev. Lett.* **118**, 040401 (2017).
39. El-Ganainy, R. et al. Non-Hermitian physics and PT symmetry. *Nat. Phys.* **14**, 11–19 (2018).
40. Shen, H., Zhen, B. & Fu, L. Topological band theory for non-Hermitian Hamiltonians. *Phys. Rev. Lett.* **120**, 146402 (2018).
41. Zhen, B., Hsu, C. W., Lu, L., Stone, A. D. & Soljačić, M. Topological nature of optical bound states in the continuum. *Phys. Rev. Lett.* **113**, 257401 (2014).
42. Doeblem, H. M., Monticone, F., den Hollander, W., Alu, A. & Koenderink, A. F. Experimental observation of a polarization vortex at an optical bound state in the continuum. *Nat. Photon.* **12**, 397–401 (2018).
43. Zhang, Y. et al. Observation of polarization vortices in momentum space. *Phys. Rev. Lett.* **120**, 186103 (2018).
44. Chen, W., Chen, Y. & Liu, W. Singularities and poincaré indices of electromagnetic multipoles. *Phys. Rev. Lett.* **122**, 153907 (2019).
45. Yin, X. & Peng, C. Manipulating light radiation from a topological perspective. *Photonics Res.* **8**, B25–B38 (2020).
46. Liu, W., Liu, W., Shi, L. & Kivshar, Y. Topological polarization singularities in metaphotonics. *Nanophotonics* **10**, 1469–1486 (2021).
47. Che, Z. et al. Polarization singularities of photonic quasicrystals in momentum space. *Phys. Rev. Lett.* **127**, 043901 (2021).
48. Zhou, H. et al. Observation of bulk fermi arc and polarization half charge from paired exceptional points. *Science* **359**, 1009–1012 (2018).
49. Chen, W., Yang, Q., Chen, Y. & Liu, W. Evolution and global charge conservation for polarization singularities emerging from non-hermitian degeneracies. *Proc. Natl Acad. Sci. USA* **118**, e2019578118 (2021).
50. Huang, C. et al. Ultrafast control of vortex microlasers. *Science* **367**, 1018–1021 (2020).
51. Zhang, X., Liu, Y., Han, J., Kivshar, Y. & Song, Q. Chiral emission from resonant metasurfaces. *Science* **377**, 1215–1218 (2022).
52. Chen, Y. et al. Observation of intrinsic chiral bound states in the continuum. *Nature* **613**, 474–478 (2023).
53. von Neuman, J. & Wigner, E. Über merkwürdige diskrete Eigenwerte. Über das Verhalten von Eigenwerten bei adiabatischen Prozessen. *Physikalische Z.* **30**, 467–470 (1929).
54. Friedrich, H. & Wintgen, D. Interfering resonances and bound states in the continuum. *Phys. Rev. A* **32**, 3231–3242 (1985).
55. Hsu, C. W. et al. Observation of trapped light within the radiation continuum. *Nature* **499**, 188–191 (2013).
56. Yang, Y., Peng, C., Liang, Y., Li, Z. & Noda, S. Analytical perspective for bound states in the continuum in photonic crystal slabs. *Phys. Rev. Lett.* **113**, 037401 (2014).
57. Hsu, C. W., Zhen, B., Stone, A. D., Joannopoulos, J. D. & Soljačić, M. Bound states in the continuum. *Nat. Rev. Mater.* **1**, 16048 (2016).
58. Jin, J. et al. Topologically enabled ultrahigh-Q guided resonances robust to out-of-plane scattering. *Nature* **574**, 501–504 (2019).
59. Sadreev, A. F. Interference traps waves in an open system: bound states in the continuum. *Rep. Prog. Phys.* **84**, 055901 (2021).
60. Kang, M., Zhang, S., Xiao, M. & Xu, H. Merging bound states in the continuum at off-high symmetry points. *Phys. Rev. Lett.* **126**, 117402 (2021).
61. Hu, P. et al. Global phase diagram of bound states in the continuum. *Optica* **9**, 1353–1361 (2022).
62. Yin, X., Jin, J., Soljačić, M., Peng, C. & Zhen, B. Observation of topologically enabled unidirectional guided resonances. *Nature* **580**, 467–471 (2020).
63. Zeng, Y., Hu, G., Liu, K., Tang, Z. & Qiu, C.-W. Dynamics of topological polarization singularity in momentum space. *Phys. Rev. Lett.* **127**, 176101 (2021).
64. Yin, X., Inoue, T., Peng, C. & Noda, S. Topological unidirectional guided resonances emerged from interband coupling. *Phys. Rev. Lett.* **130**, 056401 (2023).
65. McMaster, W. H. Polarization and the Stokes parameters. *Am. J. Phys.* **22**, 351–362 (1954).

66. Simon, B. Holonomy, the quantum adiabatic theorem, and berry's phase. *Phys. Rev. Lett.* **51**, 2167 (1983).
67. Kogelnik, H. & Shank, C. V. Coupled-wave theory of distributed feedback lasers. *J. Appl. Phys.* **43**, 2327–2335 (1972).
68. Guo, C., Xiao, M., Guo, Y., Yuan, L. & Fan, S. Meron spin textures in momentum space. *Phys. Rev. Lett.* **124**, 106103 (2020).
69. Regan, E. C. et al. Direct imaging of isofrequency contours in photonic structures. *Sci. Adv.* **2**, e1601591 (2016).
70. Liang, Y., Peng, C., Sakai, K., Iwahashi, S. & Noda, S. Three-dimensional coupled-wave model for square-lattice photonic crystal lasers with transverse electric polarization: a general approach. *Phys. Rev. B* **84**, 195119 (2011).
71. Peng, C., Liang, Y., Sakai, K., Iwahashi, S. & Noda, S. Three-dimensional coupled-wave theory analysis of a centered-rectangular lattice photonic crystal laser with a transverse-electric-like mode. *Phys. Rev. B* **86**, 035108 (2012).
72. Zhang, Y., Tan, Y.-W., Stormer, H. L. & Kim, P. Experimental observation of the quantum hall effect and berry's phase in graphene. *Nature* **438**, 201–204 (2005).
73. Pancharatnam, S. Generalized theory of interference, and its applications: part I. coherent pencils. *Proc. Indian Acad. Sci. A* **44**, 247–262 (1956).
74. Berry, M. V. The adiabatic phase and pancharatnam's phase for polarized light. *J. Mod. Opt.* **34**, 1401–1407 (1987).
75. Lee, Y.-H. et al. Recent progress in Pancharatnam–Berry phase optical elements and the applications for virtual/augmented realities. *Opt. Data Process. Storage* **3**, 79–88 (2017).
76. Xie, X. et al. Generalized Pancharatnam–Berry phase in rotationally symmetric meta-atoms. *Phys. Rev. Lett.* **126**, 183902 (2021).
77. Skyrme, T. Particle states of a quantized meson field. *Proc. Math. Phys. Eng.* **262**, 237–245 (1961).
78. Skyrme, T. H. R. A unified field theory of mesons and baryons. *Nucl. Phys.* **31**, 556–569 (1962).
79. Fert, A., Reyren, N. & Cros, V. Magnetic skyrmions: advances in physics and potential applications. *Nat. Rev. Mat.* **2**, 1–15 (2017).
80. Provost, J. & Vallee, G. Riemannian structure on manifolds of quantum states. *Commun. Math. Phys.* **76**, 289–301 (1980).
81. Anandan, J. & Aharonov, Y. Geometry of quantum evolution. *Phys. Rev. Lett.* **65**, 1697 (1990).

Acknowledgements

We acknowledge stimulating discussions with Dr. Takuya Inoue, Prof. Bo Zhen, and Dr. Jicheng Jin. This work was supported from National Key Research and Development Program of China (2022YFA1404804), National Natural Science Foundation of China (62325501 and 62135001), Grant-in-Aid for Scientific Research (22H04915).

Author contributions

X.Y. and Y.C. contributed equally to this work. X.Y. and C.P. wrote the manuscript with contributions from all authors. X.Y., C.P., and S.N. supervised the project. X.Y. designed the samples and implemented the simulations. Y.C. and Z.Z. conducted the experiments. X.Z. fabricated the samples. X.Y. and Y.C. dealt with the experiment results.

Competing interests

The authors declare no competing interests.

Additional information

Supplementary information The online version contains supplementary material available at <https://doi.org/10.1038/s41467-025-58050-8>.

Correspondence and requests for materials should be addressed to Chao Peng.

Peer review information *Nature Communications* thanks the anonymous, reviewers for their contribution to the peer review of this work. A peer review file is available.

Reprints and permissions information is available at <http://www.nature.com/reprints>

Publisher's note Springer Nature remains neutral with regard to jurisdictional claims in published maps and institutional affiliations.

Open Access This article is licensed under a Creative Commons Attribution-NonCommercial-NoDerivatives 4.0 International License, which permits any non-commercial use, sharing, distribution and reproduction in any medium or format, as long as you give appropriate credit to the original author(s) and the source, provide a link to the Creative Commons licence, and indicate if you modified the licensed material. You do not have permission under this licence to share adapted material derived from this article or parts of it. The images or other third party material in this article are included in the article's Creative Commons licence, unless indicated otherwise in a credit line to the material. If material is not included in the article's Creative Commons licence and your intended use is not permitted by statutory regulation or exceeds the permitted use, you will need to obtain permission directly from the copyright holder. To view a copy of this licence, visit <http://creativecommons.org/licenses/by-nc-nd/4.0/>.

© The Author(s) 2025